# UNIVERSITY OF BIRMINGHAM

# Laser powder bed fusion of the Ni-Mn-Sn Heusler alloy for magnetic refrigeration applications

Sun, Kun; Mohamed, Abd El-moez A.; Li, Sheng; Jeong, Minki; Head, Jake; Attallah, Moataz M.

*Document Version*
Publisher's PDF, also known as Version of record

[Link to publication on Research at Birmingham portal](#)

# Laser powder bed fusion of the Ni-Mn-Sn Heusler alloy for magnetic refrigeration applications

Kun Sun [a], Abd El-Moez A. Mohamed [a], Sheng Li [b], Minki Jeong [c], Jake Head [c], Moataz M. Attallah [a],*

[a] School of Metallurgy and Materials, University of Birmingham, B15 2TT Birmingham, United Kingdom
[b] School of Electro-mechanical Engineering, Guangdong University of Technology, 510006 Guangdong, China
[c] School of Physics and Astronomy, University of Birmingham, B15 2TT Birmingham, United Kingdom

**ABSTRACT**

This study aims to develop a manufacturing route for a low-cost dense magnetocaloric Ni-Mn-Sn Heusler alloy (HA) using laser powder bed fusion (LPBF) additive manufacturing technique by in-situ alloying from its elemental constituents. LPBF enables the production of high surface-area-to-volume 3D-printed components to increase heat transfer efficiency in magnetic refrigerators. A laser parametric study was performed on blocks, lattices and microchanneled cylinders for maximum densification, the highest density was observed at the samples with laser energy density ($E_V$) of 18.52 J/mm$^3$, 53.33 J/mm$^3$ and 89.89 J/mm$^3$, where they achieved a density of 6.8 g/cm$^3$, 8.2 g/cm$^3$ and 8.3 g/cm$^3$, respectively. After heat treatment, the three samples show the L2$_1$ phase with a minor 4 O orthorhombic phase and double magnetic transitions, martensitie-austenite transition ($T_M$) and curie temperature ($T_C^A$). The maximum magnetic entropy change ($\Delta S_{max}$) values of the three samples around $T_M$ are 0.53 Jkg$^{-1}$ K$^{-1}$ at 160 K, 0.5 Jkg$^{-1}$ K$^{-1}$ at 130 K, and 0.3 Jkg$^{-1}$ K$^{-1}$ at 170 K, respectively. And $\Delta S_{max}$ of almost 1.0 Jkg$^{-1}$ K$^{-1}$ at $T_C^A$ (~320 K) for these samples with a field change of 1 T.

## 1. Introduction

Magnetic refrigeration is a promising environmentally friendly technology that may help in addressing global warming and energy challenges around the world. Compared with conventional cooling systems, magnetic refrigeration devices emit less mechanical noise and vibrations [1,2], and theoretically achieve higher energy efficiency (60% of Carnot cycle) [2]. Magnetic refrigeration is based on the magnetocaloric effect (MCE), which is a change in the magnetic entropy ($\Delta S$) upon applying/removing an external magnetic field, resulting in a temperature change ($\Delta T$) [1,3], where $\Delta S$ and $\Delta T$ are being maximum around the magnetic transition temperature. The MCE has been observed in several magnetic materials, however, Gd has been reported with the highest room temperature MCE [4], but the high cost of that metal hinders its wide usage in applications. So it was important to look for alternatives such as rare earth-based composites and Huesler alloys, which are outstanding magnetocalorics with environmentally friendly effects, lower cost and adjustable magnetic transition temperature [4,5]. These magnetocaloric materials (MCMs) have been prepared via

different synthesis methods such as arc melting [5,6] and powder metallurgy [7], …etc. The main problem of resultant samples from these traditional methods is the lack of shaping to suit a specific application, which is a challenge of being machined after fabrication due to the weak mechanical strength of these materials [8]. Additive manufacturing (AM) technology such as LPBF has overcome the challenge of machining by direct part production with the ability to do complex designs, where components are designed using computer-aided design software and then built from a raw powder in a layer-by-layer fashion [9]. However, the microstructure defects such as cracking and porosity cannot be avoided during the LPBF process, so laser parameters optimisation is needed [10–12]. LPBF has been used previously in 3D printing of several functional magnetic materials such as, AlFe$_2$B$_2$ alloy [13], CoFeNi [14–16], FeNi [17], functionally graded magnetic materials [18] and in particular MCMs such as LaCe(Fe,Mn,Si)$_{13}$ [11], La(Fe,Co,Si)$_{13}$ [8] (Mn, Fe)$_2$(P,Si) [18]. These reported works have shown the important role of 3D printing of MCMs in improving magnetic refrigeration efficiency. This occurred by producing parts with high surface-area-to-volume, which improves the heat transfer between the heat source, working

---

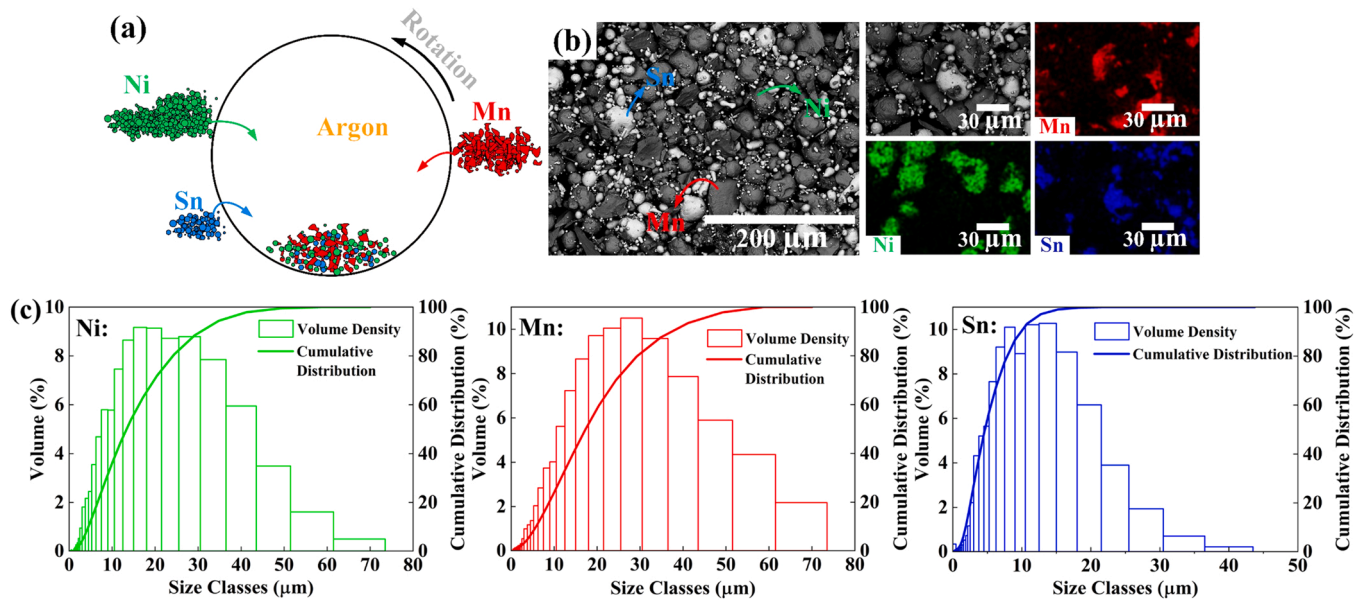**Fig. 1.** (a) Schematic illustration of the powder blending process, (b) backscattered electron image and corresponding EDS elemental map of the $Ni_{50}Mn_{37}Sn_{13}$ blended powder, (c) Particle size distribution of the three powders.

**Table 1**
Starting raw powder characteristics.

| Elements | Particle size range (μm) | d50 (μm) | Shape of powder | Melting point (°C) | Boiling point (°C) | Density (g/cm³) |
|----------|--------------------------|----------|-----------------|--------------------|--------------------|------------------|
| Ni | 20–45 | 0.38 | Spherical | 1455 | 2913 | 8.9 |
| Mn | < 44 | 2.01 | Cubic | 1426 | 2061 | 7.44 |
| Sn | < 45 | 0.74 | Spherical | 232 | 2602 | 6.54 |

body and sink [19]. Controlling the heat transfer by increasing the surface area of MCMs by 3D printing was reported previously in LPBF and laser beam melted La-Fe-Si based alloy [8,11,20,21]. They produced blocks with internal micro-wavy channels [8] and blocks with straight microchannels and lattices [11]. Despite the outstanding role of LPBF of MCMs, some challenges have been reported such as the elemental evaporation that may interrupt the nominal chemical composition of the magnetic alloy, leading to a disturbance in the associated magnetic properties [11]. This challenge can be overcome by optimising laser parameters, using relatively lower laser energy densities and compensating the evaporated elements. Despite the interesting magnetic properties of La-Fe-Si, HAs have been reported with the same $\Delta S$ at a much lower cost, which make this category a kind of interest for applications, especially at room temperature [6,7]. HAs Ni-Mn-X(In, Sn, …etc) show a huge MCE associated with the martensitic transition [22]. In addition, these alloys show a conventional MCE at the austenite phase transition, which can be used as a double cooling capacity [23]. Among this category, Ni-Mn-Sn shows a near-room temperature magnetic transition, which makes this alloy a kind of interest [22,24]. Only one work has been reported in the 3D printing of Ni-Mn-Sn using LPBF technique [10]. This work used a pre-alloyed powder to manufacture parts with hexagonal/square/circular macro channels (3 mm) inside were built by using LPBF pre-alloy Ni-Mn-Sn powders, with reported magnetic properties of $\Delta S$ of 1.4 Jkg⁻¹ K⁻¹ at 288 K and 1 T [10].

This study aims to manufacture high-performance MCE prototypes of $Ni_{50}Mn_{37}Sn_{13}$ HAs using LPBF in situ alloying as a low-cost approach and an alternative to the pre-alloyed powder. A series of experiments were designed to study the influence of the process parameters on the microstructure development of the in-situ alloyed Ni-Mn-Sn block samples. Microchanelled cylinders and lattice strut samples were also

manufactured to increase the surface-area-to-volume of the components, which can maximise heat transfer efficiency.

## 2. Material and methods

### 2.1. Powder preparation

The $Ni_{50}Mn_{37}Sn_{13}$ alloy was prepared by in-situ alloying as seen in Fig. 1a of spherical gas atomised Ni powder (TLS Technik GmbH, Germany, Purity $\geq$ 99.5%), spherical Sn powder (Sigma-Aldrich, USA, Purity $\geq$ 99.8%) and irregular Mn powder (Aldrich, USA, Purity $\geq$ 99%), see Fig. 1b. Additional 2 at% Mn and 1 at% Sn powders were added to compensate for the elemental evaporation during LPBF process, which was observed following initial trials. Ni, Mn, and Sn powders were blended for 48 h. The particle size distribution for all powder is presented in Fig. 1c and details are listed in Table 1, which is following a Gaussian distribution.

### 2.2. Sample fabrication and design of experiment

The as-fabricated (AF) samples were manufactured by LPBF technique on top of steel substrate using Concept Laser M2 machine attached with a continuous wave mode Yb-fibre laser (spot size is $\approx$ 67 μm, maximum power = 400 W) as the primary heat source for melting in argon atmosphere with the oxygen content kept below 1000 ppm.

Three designs were optimised, $5 \times 5 \times 10$ mm blocks, body-centered cubic (BCC) strut-based lattice structure and cylinders with microchannels (MC cylinders) (see Fig. 2a-b) using a fixed layer thickness of 30 μm. The details of the three designs are shown in Fig. 2c-d. Among the parameters in the LPBF process, the effective laser power (P), the laser scan speed (V), the laser scan spacing or hatch distance (h), and the layer thickness (d) are the most important in controlling the build integrity [25]. Different scanning strategies were used as shown in Fig. 3. During the LPBF process, the volumetric energy density ($E_V$) is used to define the effective laser energy or linear energy density ($E_L$) using the key process parameters, as given by Eq.1 and Eq.2 [26]:

$$E_v = \frac{P}{V \bullet h \bullet d} \tag{1}$$
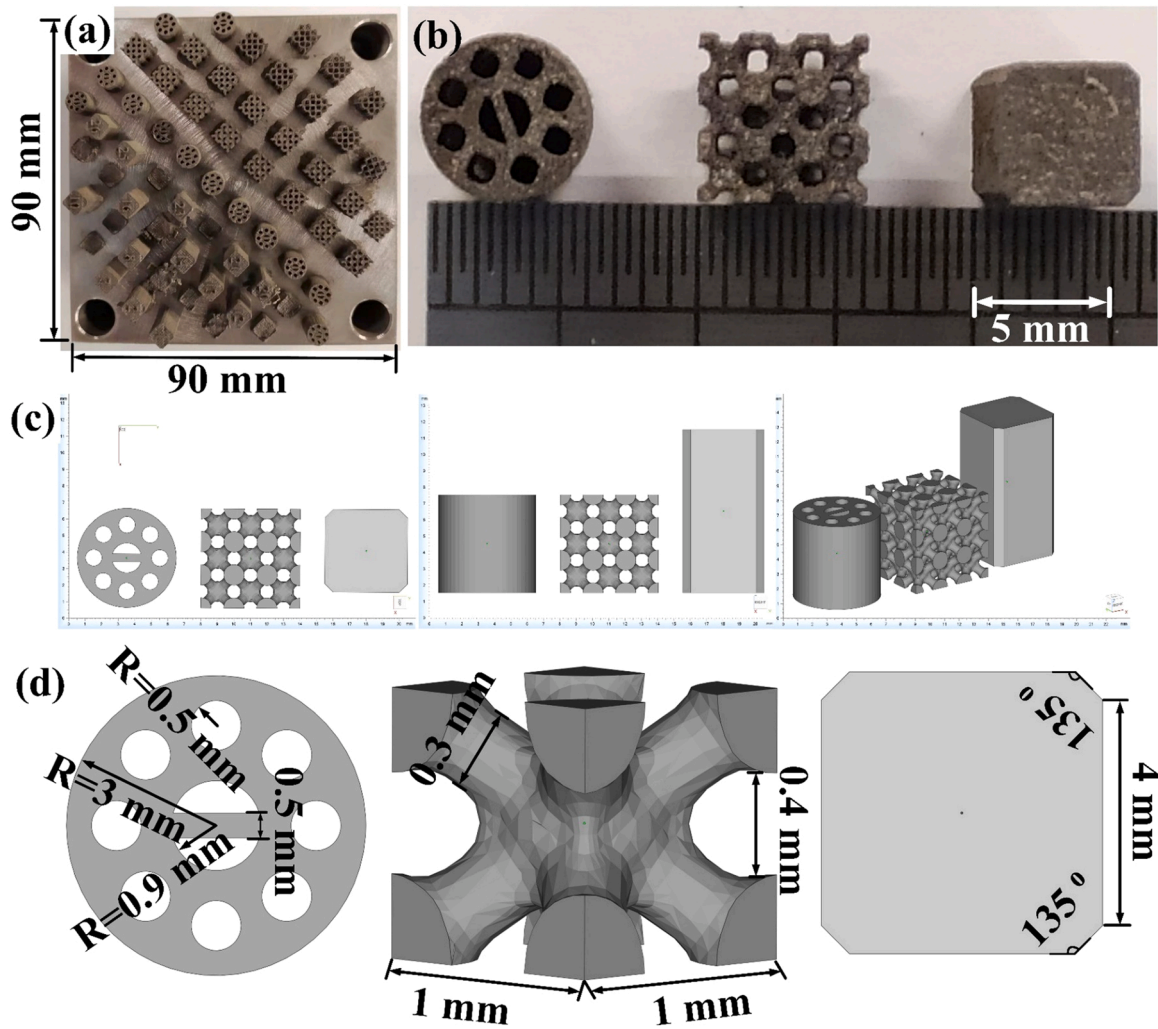
**Fig. 2.** (a) and (b) LPBFed parts, (c) Geometry of blocks, lattices, and microchannel cylinders, (d) Details of three different designs.
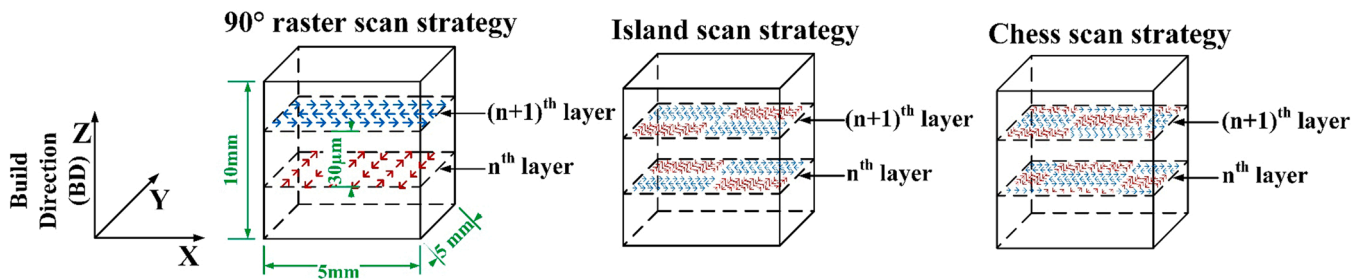


**Fig. 3.** Three different scan strategies; 90° raster, island scan and chess scan strategies.

**Table 2**

The investigated LPBF processing parameters for blocks with the 90° raster scan strategy.

| Laser Power (W) | Scan Speed (mm/ s) | Hatch Distance (mm) | Energy Density (J/ mm³) |
|---|---|---|---|
| 60–150 | 600–1500 | 0.03–0.09 | 18–133 |

$$E_L = \frac{P}{V} \qquad (2)$$

The optimisation process for maximum densification was performed on blocks using the parametric combinations detailed in Table 2. The results of the microstructure of blocks assessed with continued scanning strategies, parameters (shown in Table 3) were observed to build satisfactory blocks with island and chess scanning strategies (with an island size of 3 ×3 mm), MC cylinders and lattices.

The LPBF made (LPBFed) samples were encapsulated in argon-filled quartz ampules and heat-treated (HT) in a calibrated furnace at 1123 K for 504 h before water quenching.

**Table 3**

The LPBF processing parameters for blocks with island and chess scan strategies, MC cylinders, and lattices. ($\sqrt{}$: Succeed; $\times$: Failed).

| Laser Power (W) | Scan Speed (mm/s) | Hatch Distance (mm) | $E_V$ (J/mm$^3$) | $E_L$ (J/mm) | Chess Blocks | Island | 90° Raster Scan Strategy MC Cylinder | Lattice |
|---|---|---|---|---|---|---|---|---|
| 60 | 600 | 0.05 | 66.67 | 0.1 | $\sqrt{}$ | $\sqrt{}$ | $\sqrt{}$ | $\sqrt{}$ |
| 60 | 600 | 0.07 | 47.61 | 0.1 | $\sqrt{}$ | $\sqrt{}$ | $\sqrt{}$ | $\sqrt{}$ |
| 60 | 800 | 0.07 | 35.71 | 0.075 | $\sqrt{}$ | $\sqrt{}$ | $\sqrt{}$ | $\sqrt{}$ |
| 60 | 1000 | 0.05 | 40 | 0.06 | $\sqrt{}$ | $\sqrt{}$ | $\sqrt{}$ | $\sqrt{}$ |
| 70 | 1000 | 0.05 | 46.67 | 0.07 | $\sqrt{}$ | $\sqrt{}$ | $\sqrt{}$ | $\sqrt{}$ |
| 80 | 1000 | 0.05 | 53.33 | 0.08 | $\sqrt{}$ | $\sqrt{}$ | $\sqrt{}$ | $\sqrt{}$ |
| 80 | 600 | 0.07 | 63.49 | 0.13 | $\times$ | $\times$ | $\times$ | $\sqrt{}$ |
| 115 | 1750 | 0.05 | 43.8 | 0.065 | $\times$ | $\times$ | $\sqrt{}$ | $\sqrt{}$ |
| 115 | 2000 | 0.05 | 38.33 | 0.057 | $\times$ | $\times$ | $\sqrt{}$ | $\sqrt{}$ |
| 125 | 1500 | 0.06 | 46.29 | 0.083 | $\times$ | $\times$ | $\sqrt{}$ | $\sqrt{}$ |
| 125 | 1750 | 0.05 | 47.62 | 0.071 | $\times$ | $\times$ | $\sqrt{}$ | $\sqrt{}$ |
| 125 | 2000 | 0.04 | 52.08 | 0.063 | $\times$ | $\times$ | $\sqrt{}$ | $\sqrt{}$ |
| 125 | 2500 | 0.045 | 37.04 | 0.05 | $\times$ | $\times$ | $\sqrt{}$ | $\sqrt{}$ |
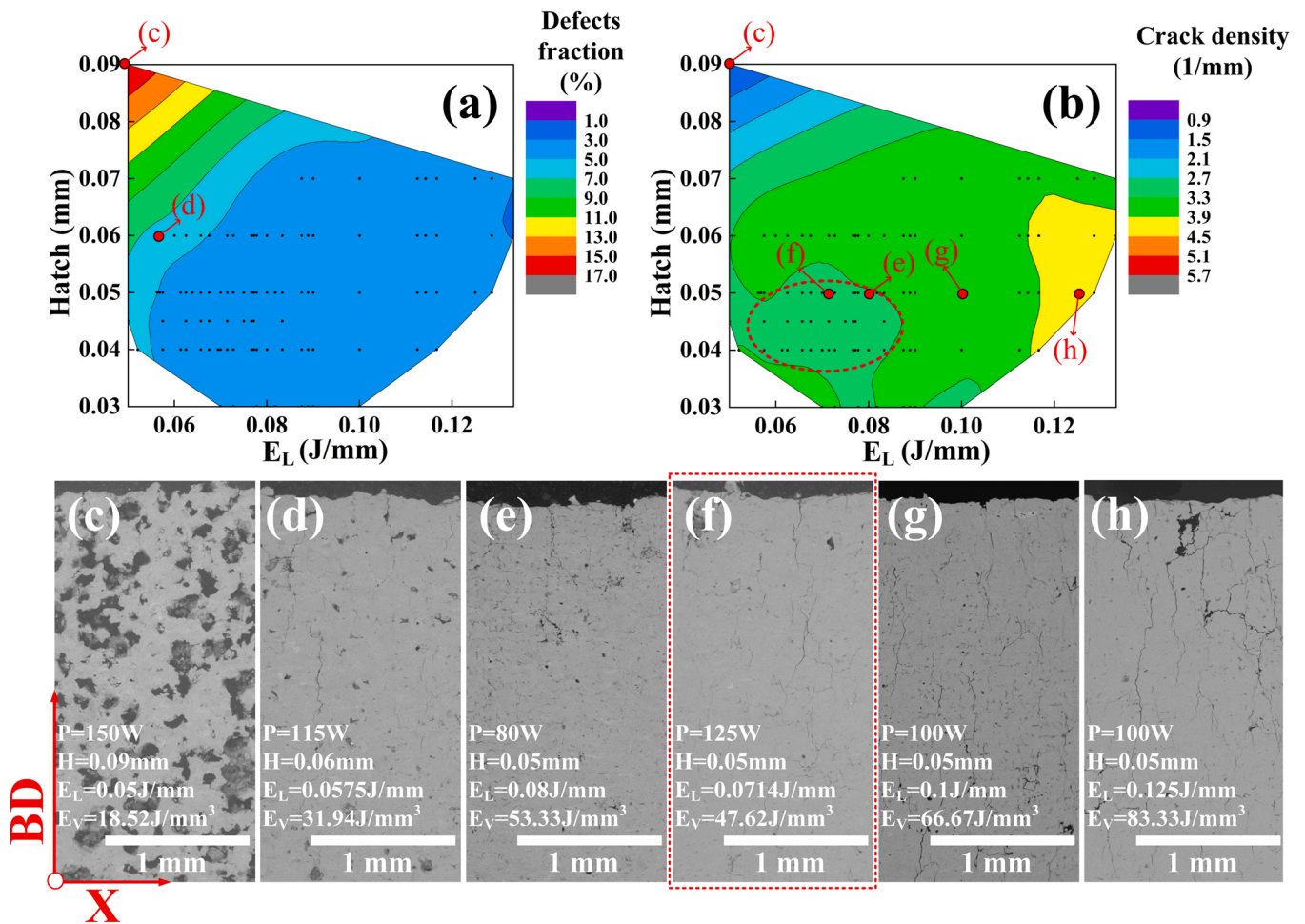


**Fig. 4.** The correlation of $E_L$ and Hatch with the (a) Defects fraction, and (b) Crack density of all AF blocks with 90° raster scan strategy.

### 2.3. Sample preparation and analysis

The Ni-Mn-Sn samples were cut from the steel substrate using Electrical Discharge Machine (EDM). The samples were then sectioned longitudinally to the build direction (to view the X-Z plane). The density of samples was measured using the Archimedes method in terms of ASTM B962–17 [27]. The samples were ground incrementally using SiC papers and then polished using 3 and 1 μm diamond suspensions, finishing with a 0.04 μm silica suspension. Then, Hitachi TM3030 and FEI Quanta 3D FEG Dual Beam SEM fitted with an Energy Dispersive X-ray microanalysis system (EDS) microscopes were used to analyse the microstructure of the polished samples. Image analysis using Image J software was used to quantify the defects fraction (defects area/area, %) and cracking density (sum of cracks length/total image area, 1/mm) [28]. 8 SEM images in the X-Z plane were considered for every sample at the mid-thickness of the Y-Z section. The crystal structure was examined using a Proto AXRD diffractometer X-ray diffraction (XRD) with Cu-Kα radiation (λ = 1.5406 Å) at room temperature and using a Panalytical Empyrean XRD diffractometer with Mo-Kα radiation (λ = 0.7093 Å) for the tests at low temperature (100 K, 200 K and 295 K). For comparison,
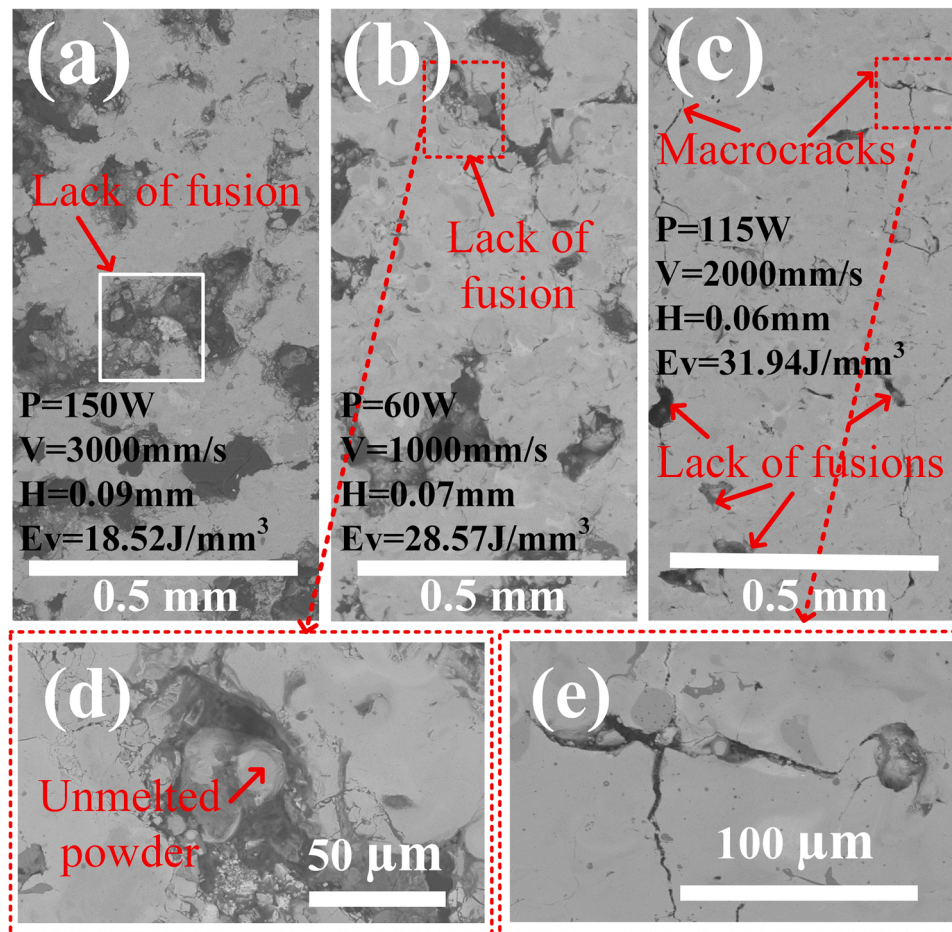
**Fig. 5.** SEM-BSE micrographs showing the defects in the sample with low energy density.
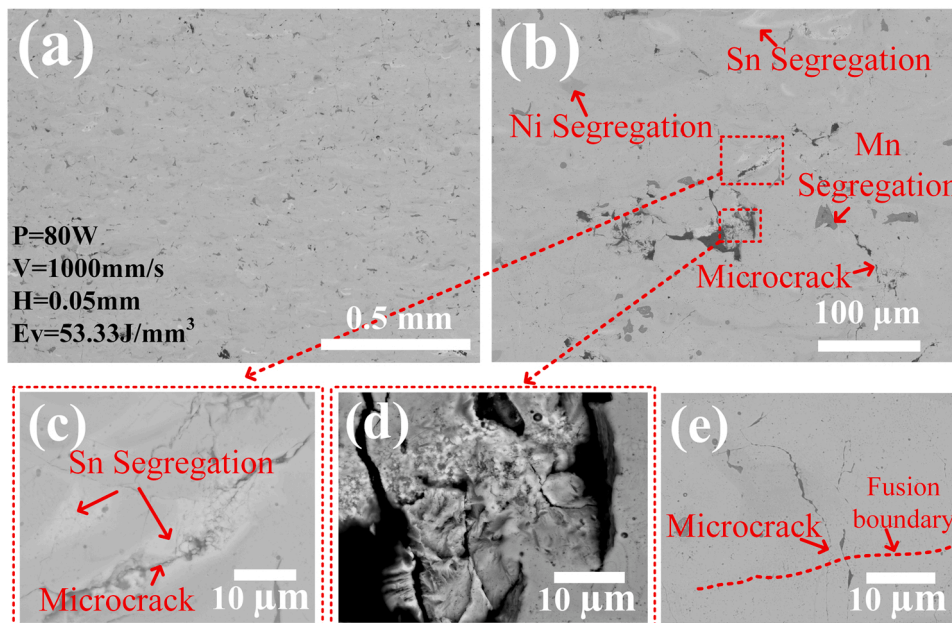


**Fig. 6.** SEM-BSE micrographs showing the defects in the best sample (No.2-AF).

all XRD results with Mo-Kα radiation were converted to Cu Kα radiation using Bragg's Law. The chemical compositions of ten small uniform areas within the microstructure, without element segregation, of every

sample were confirmed using the FEI Quanta 3D FEG Dual Beam SEM-EDS. The average composition was then used to represent the chemical composition of all uniform areas. The chemical composition of

**Fig. 7.** SEM-BSE micrographs showing the defects in the sample with high energy density.

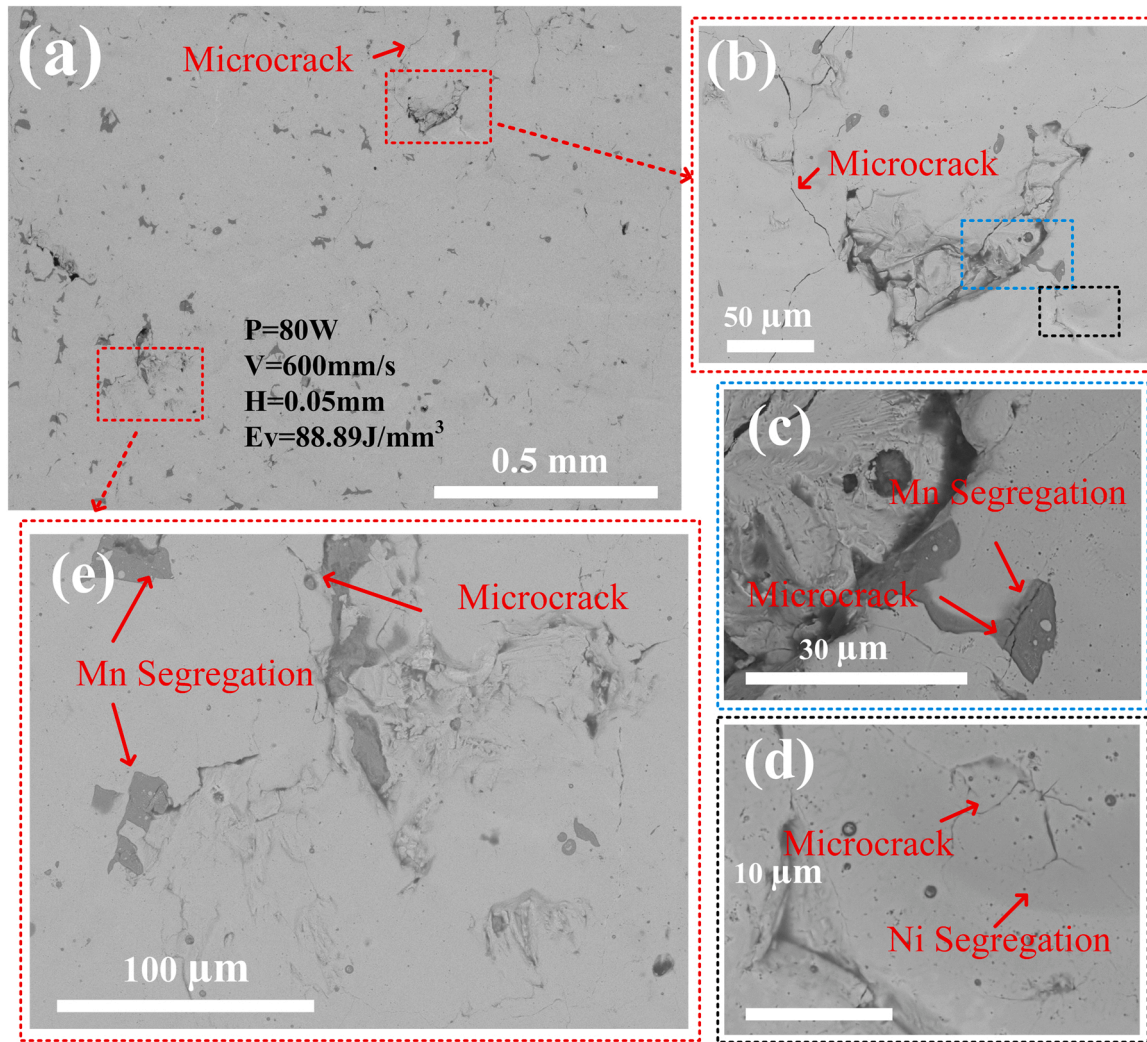the whole sample was determined using x-ray fluoresce (XRF) for Ni, Mn, and Sn, and combustion and non-dispersive single wavelength IR analysis for Oxygen analysis.

Magnetic measurements were performed using a Quantum Design Magnetic Property Measurement System (MPMS). All test samples were extracted from the centre of the blocks. The zero-field cooled heating (ZFCH) thermo-magnetisation data were collected under 0.01 T within the temperature range of 2–380 K. The isothermal magnetisation curves were measured every 5 K (field up from 0 to 1 T, then back to 0 T). The magnetic entropy change ($\Delta S$) was calculated from the isothermal magnetisation curves M(H) using Maxwell's relation (Eq.3). The change in the applied magnetic field is represented by $\Delta H$ ($\Delta H = H_F - H_I$, $H_F$: the final magnetic field; $H_I$: the initial magnetic field).

$$\Delta S = \int_{H_I}^{H_F} \left( \frac{\partial M}{\partial T} \right)_H dH \tag{3}$$

The RCP of MCMs can be evaluated from the plots of $\Delta S$ vs T, as shown in Eq. 4. $\delta T_{FWHM}$ is the full width at half maximum of $\Delta S$(T) curve [2].

$$RCP(S) = \Delta S_{max} \times \delta T_{FWHM} \tag{4}$$

## 3. Results and discussion

### 3.1. Microstructure of the as-fabricated samples

To identify the processing windows that achieved the least pores and cracks, contour plots were constructed. As shown in Fig. 4a-b, the volumetric defects fraction (%) and crack density (crack length/area, 1/ mm) were plotted against the $E_L$. The blocks with low $E_L$ and high hatch saw a high quantity of defects and a low number of cracks due to a large number of interconnected holes within the blocks possibly releasing the residual stress during LPBF processing, decreasing the level of cracking, as illustrated in Fig. 4c.

The quantity and size of the holes decreased with the increasing $E_L$ and decreasing hatch, as shown in Fig. 4d. The results presented in Fig. 4e-f display a denser microstructure yet with some cracks. Fig. 4g-h revealed huge macrocracks because high $E_L$ and low hatch result in high $E_V$. The cracking density increases with the increasing residual stress caused by the increasing energy density. Although it was difficult to fully eliminate the defects, especially cracking, a narrow processing window resulted in a lower density of defects and cracks, as shown in the red cycle within Fig. 4b. It was established that the condition of $E_V$= 53.33 J/mm$^3$ (80 W, 1000 mm/s and 0.05 mm, Fig. 4e) showed the lowest defects and cracks fraction and the suitable densification. Thus, this condition is recommended as the optimum condition for block samples.
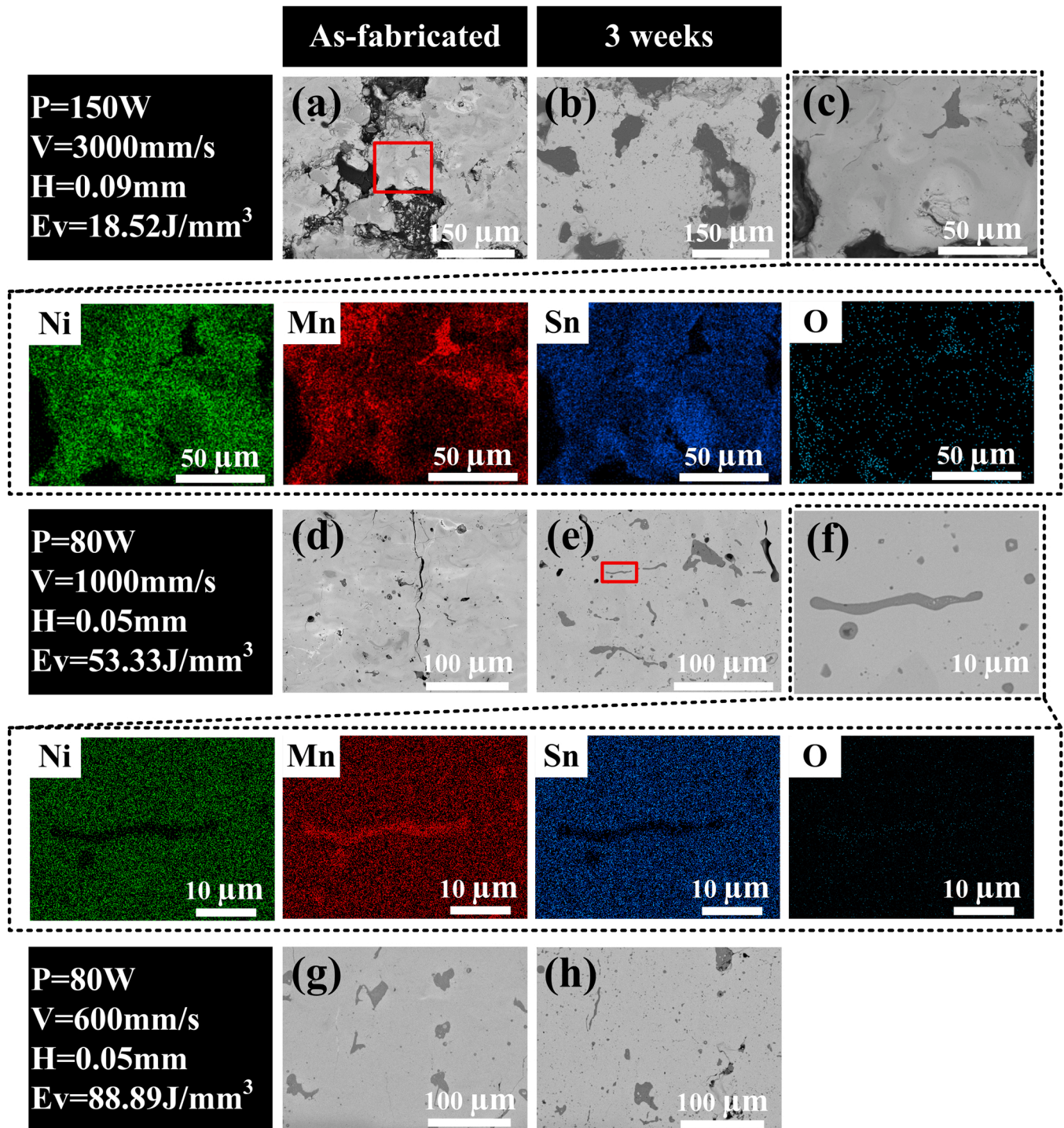
**Fig. 8.** SEM-BSE micrographs showing microstructure of LPBFed samples (a, c, d, and g) and HT LPBFed samples (b, e, f, and h), and EDS map for Ni, Mn and Sn element segregations in LPBFed and HT LPBFed samples.

### 3.2. Microstructure evolution and defects mechanism

Fig. 5, Fig. 6 and Fig. 7 show the SEM-BSE micrographs of selected block samples, which document the microstructural evolution with increasing $E_V$. Three segregations were observed in the microstructure of the samples. Ni segregation is grey, Mn segregation is dark grey and Sn segregation is white in the SEM-BSE picture (proved in Fig. 9). As shown in Fig. 5a-c, the high defects, especially some of the irregularly formed pores, at low $E_V$ of 18.52, 28.57 and 31.94 J/mm$^3$ was due to the insufficient overlap between the laser tracks caused by the large hatch

spacing (90 μm), insufficient melting caused by lower laser power, and unsuitable scanning speed. The lack of fusion defects (LOFs) and un-melted powders are very common within the microstructure of blocks with low $E_V$, as shown in Fig. 5d and e, resulting in low density and relative density (see Fig. 8 and Fig. 9). With increasing $E_V$, the un-melted powder caused by the LOFs almost disappears. The macrocracks were observed in the microstructure of the sample ($E_V$ = 31.94 J/mm$^3$).

Fig. 6 presented the defects of the best sample (No.2-AF). Still, a large number of cracks could also be observed, where the cracks have grown in a zig-zag movement. Some cracks occurred within the Sn segregation,
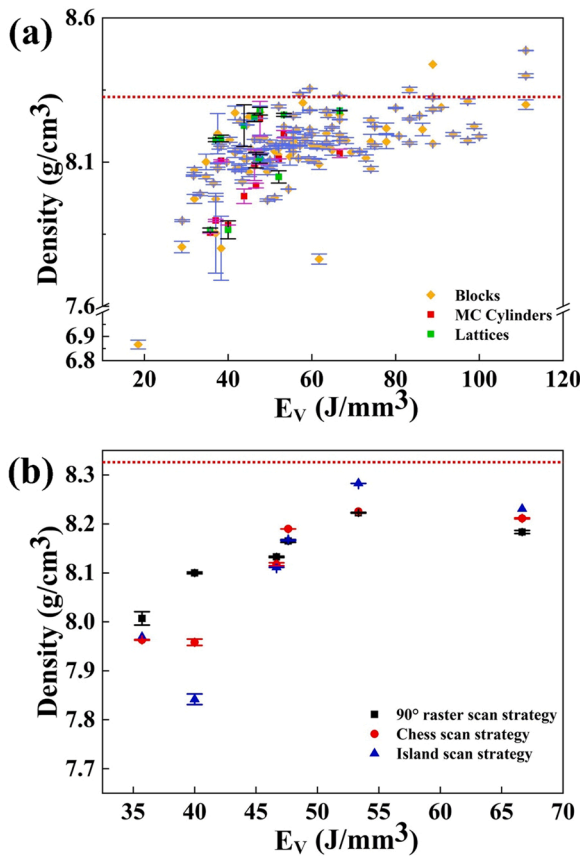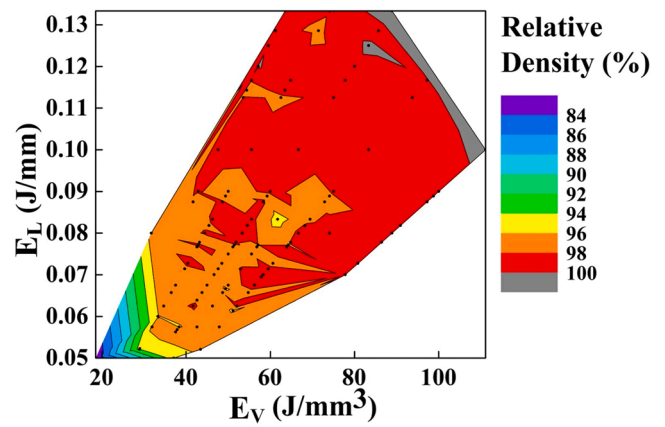
**Fig. 10.** The relationship of $E_V$, $E_L$, and the relative density of all AF blocks with 90° raster scan strategy.

see Fig. 6c. The small LOFs were also observed (Fig. 6d). It is caused by the liquid metal solidifying rapidly during the LPBF process. Furthermore, some cracks grow mostly through the fusion boundary (Fig. 6e).

Fig. 7 presented the defects within the microstructure of the sample with high energy density. The microcracks are obvious (Fig. 7a and b). Some microcracks occurred within the Mn segregation region (Fig. 7c) and the Ni segregation region (Fig. 7d).

### 3.3. Influence of post-LPBF thermal quenching post-process on the microstructure

Fig. 8 shows SEM-BSE micrographs of the AF (a, c, d and g) and HT samples (b, e, f and h). Details of the LPBF and heat treatment processing parameters for picked blocks (No.1, No.2, and No.3) are shown in Table 4. The corresponding AF samples are No.1-AF, No.2-AF, and No.3-AF. The micrographs show some segregations: Sn (bright), Mn (dark grey) and Ni (light grey). Heat treatments typically promote microstructural homogeneity by decreasing segregation, especially Sn segregation due to its lower melting point (231.9 ℃) than the HT temperature. There is some remnant segregation of Ni and Mn.

Different LPFB parameters caused different evaporation rates, which lead to the samples having different chemical compositions. Table 5 shows the average chemical composition (including the electro-to-atom ratio; e/a) of the uniform area, without any segregation, in the three samples following the HT process. The HT processes and three different LPBF parameters did not result in a big difference in the average composition. Table 6 shows the average chemical composition (including Oxygen) of the whole No.1 and No.3 samples.

### 3.4. Density

In terms of the chemical composition, the theoretical density of the investigated Ni-Mn-Sn alloy should be 8.326 g/cm³ (the red-dotted line shown in Fig. 8), which was used as a reference for all specimens. Fig. 8a shows the influence of $E_V$ on the Archimedes density of the AF specimens. When $E_V$ is less than 30 J/mm³, the density is very low due to the large fraction of LOFs that occurred in the block, as shown in Fig. 4c. When $E_V$ is very high (>100 J/mm³), selective elemental vaporisation of Mn increases the density of the blocks because the density of Mn is lower than that of Ni and Sn. As observed in Table 3, high P or $E_L$ will result in failed blocks with chess and island scan strategies. Since $E_L$ density at the edge of a short raster scan within the chess and island scanned blocks was so high the melted powder in that area was thicker and other points in the same layer had less time to cool down. In addition, the residual stress and heat input also accumulated with the increasing number of printing layers. Fig. 9b shows that the three different scan strategies

**Fig. 9.** (a) Influence of $E_V$ on density, (b) Influence of laser scan strategy on the AF block density.

**Table 4**
The LPBF and heat treatment processing parameters for picked blocks.

| No. | Laser Power (W) | Scan Speed (mm/s) | Hatch Distance (mm) | $E_V$ (J/ mm³) | Scan Strategy | Heat Treatment Process |
|---|---|---|---|---|---|---|
| No.1 | 150 | 3000 | 0.09 | 18.52 | 90° raster scan strategy | 950 ℃−504 h-Quench |
| No.2 | 80 | 1000 | 0.05 | 53.33 | | |
| No.3 | 80 | 600 | 0.05 | 88.89 | | |

**Table 5**
Average chemical composition analysis in at% of the HT block samples using SEM-EDS.

| | Ni | Mn | Sn | e/a |
|---|---|---|---|---|
| Initial Mixed Powder | 48.54 | 37.86 | 13.59 | |
| No.1 (18.52 J/mm³) | 49.14 | 34.7 | 16.16 | 7.99 |
| No.2 (53.33 J/mm³) | 48.80 | 33.91 | 17.29 | 7.95 |
| No.3 (88.89 J/mm³) | 49.25 | 34.22 | 16.53 | 7.98 |

**Table 6**
Chemical composition analysis (including oxygen analysis using LECO) in at% for the HT block samples.

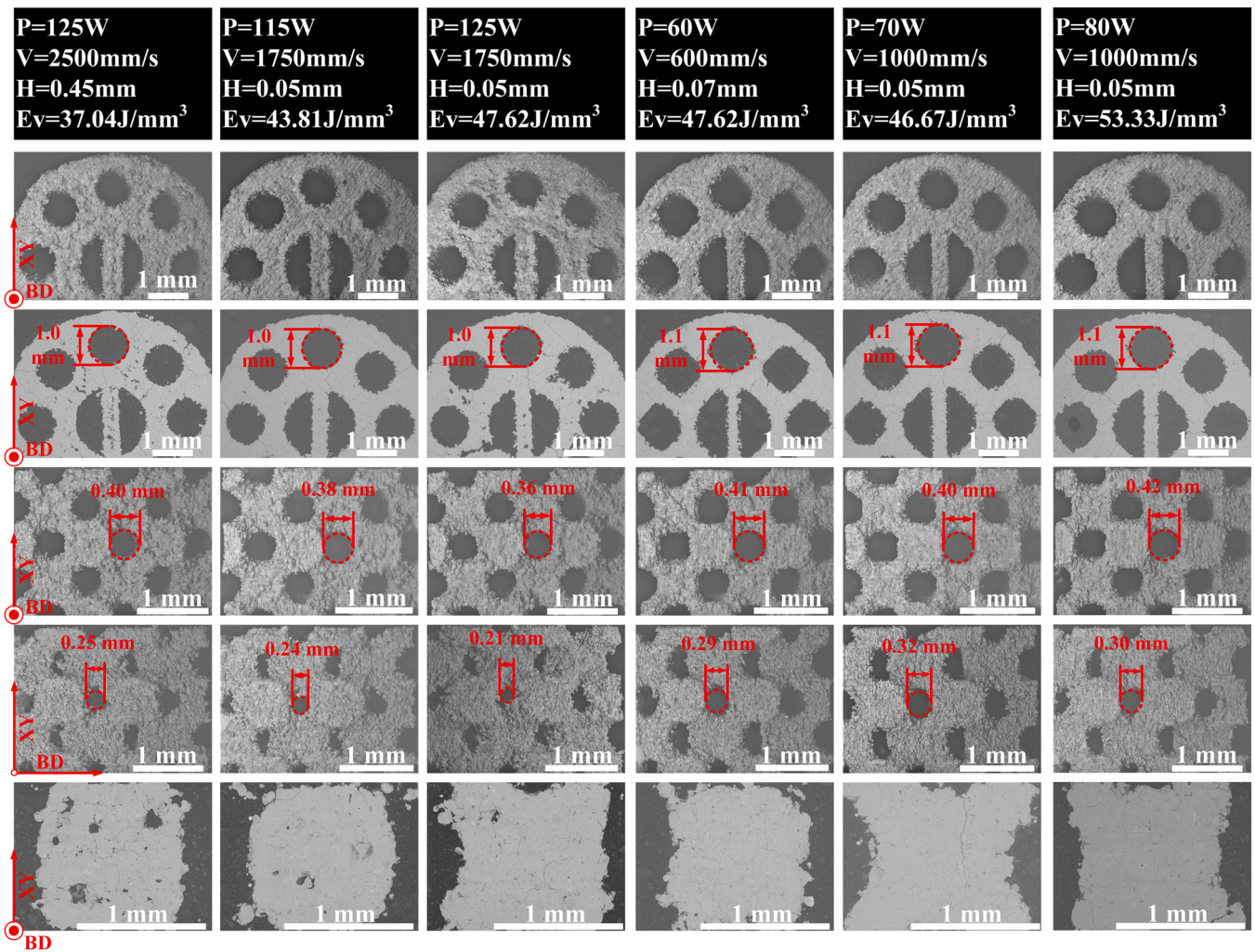| | Ni | Mn | Sn | O |
|---|---|---|---|---|
| No.1 (18.52 J/mm³) | 46.95 | 33.50 | 13.50 | 6.00 |
| No.3 (88.89 J/mm³) | 49.20 | 32.90 | 14.6 | 3.00 |

**Fig. 11.** SEM-BSE micrographs showing surface morphologies (X-Y) and microstructure of cylinders with the microchannels (red circles); SEM-BSE micrographs showing surface morphologies (X-Y/Y-Z) and microstructure lattice strut samples.
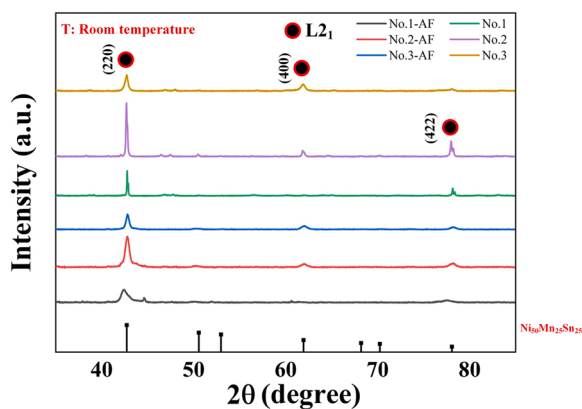


**Fig. 12.** XRD patterns of the LPBFed and HT LPBFed Ni-Mn-Sn alloys.
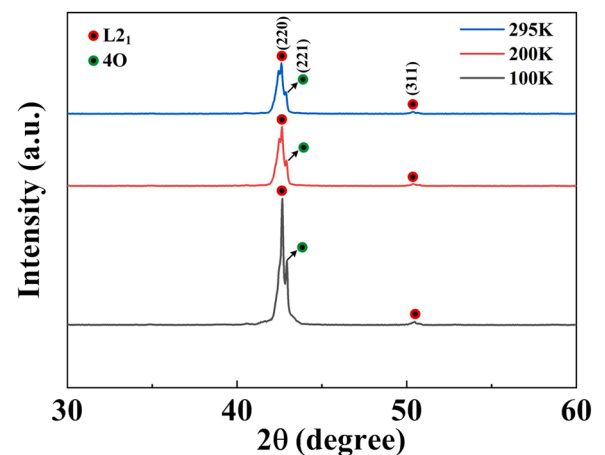


**Fig. 13.** XRD patterns of the HT LPBFed Ni-Mn-Sn (No.2) at different temperatures (100 K, 200 K, 295 K).

didn't result in a huge variation in density ($<0.25$ g/cm$^3$). As shown in Fig. 10, the relative density of some LPBFed blocks, with high $E_V$ and $E_L$ was above 100%, indicating that the density is higher than the theoretical density. This has occurred because high P and $E_L$ will result in elemental evaporation, which will change the chemical composition and increase the density of the blocks.

The surface morphologies of the MC cylinders (X-Y, normal direction) and lattices, and the cross-sectional (X-Y) microstructure of both parts, produced using six different LPBF process parameters, are shown in Fig. 11. The surface of MC cylinders and lattices contains some partially melted residual powder particles as a result of the LPBF process

**Fig. 14.** Thermo-magnetisation curves of HT LPBFed Ni-Mn-Sn samples in an applied field of 0.01 T.

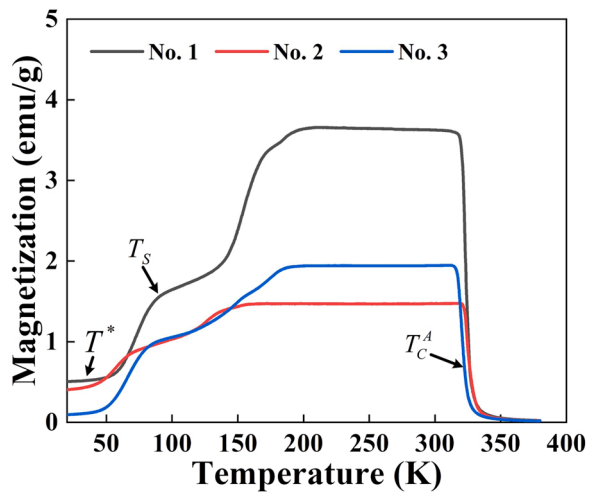[29]. The $E_V$ did not significantly change (37 J/mm$^3$ to 53 J/mm$^3$), but the laser power changed considerably (60–125 W). Although the size of MC cylinders and lattices is small, cracks can be seen in all the specimens. More LOFs and pores were observed in the microstructure of MC cylinders and lattices produced by using high laser powder (>115 W) because of increased splashing and a high cooling speed. The Image J software was used to determine the effective diameters. The diameter of the holes in MC cylinders (1.0 mm) and X-Y plane of lattice structures (0.4 mm) was built relatively accurately. However, the holes in the Y-Z plane of lattice structures were not accurate. The diameter of the holes is small (~0.24 mm) when using high-laser power. The high laser power tended to block the pores (especially the surface morphology Y-Z, build direction) due to the wider melt pool and deeper melt depth resulting in more powder sticking to the channels. The MC cylinders and lattices produced by using lower laser powder saw more recognisable, uniform pore morphology and fewer pores within the microstructure. Therefore, it can be concluded that low laser power (60, 70 and 80 W) is more suitable for manufacturing MC cylinders and lattices when using the 90° raster scan strategy.

### 3.5. Influence of post-LPBF thermal quenching post-process on the phase formation

Fig. 12 shows the XRD patterns of the HT LPBFed Ni-Mn-Sn samples at room temperature (RT). The images reveal the dominance of the L2$_1$ austenite phase in all samples at RT. In contrast, a 4-layered orthorhombic (221) peak was visible near the austenite (220) peak, revealing the coexistence of the 4 O-type martensite phase at low temperatures (100 K) [30,31], which decreases with increasing the temperature (see Fig. 13). Chemical composition plays an important role in the martensite phase volume and transition, where it has been reported that HAs with a chemical composition of Ni$_{50}$Mn$_{50-x}$Sn$_x$ (x = 13–15) show strong 4 O and martensite phase peaks [32,33]. The samples analysed had a low-intensity 4 O martensite peak as a result of deviation of the chemical composition (See Table 5) from the optimum starting values, due to evaporation and the microstructural inhomogeneity.

### 3.6. Magnetic properties

#### 3.6.1. Temperature dependence of magnetisation

Fig. 14 shows the thermal variation of magnetisation for the three blocks, the M(T) behaviour agrees with the previous studies of arc-melted Ni-Mn-Sn alloys [30]. At high temperatures (340–400 K), the magnetisation value is close to zero due to the paramagnetic state in the

austenite phase. By decreasing the temperature below 340 K, the three samples exhibit a sudden increase in the magnetisation in correspondence with the paramagnetic (PM)–ferromagnetic (FM) transition at $T_C^A$ (~320 K). The ($T_C^A$) value agrees with the previously reported values in the arc-melted Ni-Mn-Sn alloys [33]. A further decrease in temperature leads to a decrease in magnetisation (antiferromagnetic behaviour) due to the start of the Martensitic transition, in agreement with [30]. Magnetisation continued to decrease with temperature showing a step-like anomaly around Ts before remaining constant below T * (~50 K). The observed difference in the magnetisation behaviour in the austenite and martensite phases refers to the change in Mn-Mn distance [34] where, the Mn-Mn distance decreases after the martensitic transformation due to the twining of the martensitic phase [35] inducing an antiferromagnetic (AFM) coupling component [6,36]. The presence of the AFM component has been reported previously in Ni-Mn-Sn alloys and is attributed to the existence of ferromagnetic particles/grains, which are in a non-magnetic order [37] with inhomogeneous magnetic states [38]. The presence of the AFM component increases with a decrease in temperature and leads to FM-AFM competition, locking spins from the contribution in magnetisation, which explains the constant value of M below T* [30,39]. It is worth noting that the three samples show different magnetisation values, which may occur due to the change in chemical composition resulting from the different processing parameters (see Table 5 and Table 6). The lower Ni and Sn contents lead to some of the Mn ions occupying Ni and Sn sites, which are coupled antiferromagnetically to those on the regular Mn sites, and lead to the AFM interaction [34,40]. Accordingly, the lower Ni and Sn content in sample No. 1 led to the highest magnetisation. It is worth to mention that Ni-Mn-Sn alloys have shown small thermal magnetic hysteresis 5 K in previous works of arc melted [41] and 5 K in HT LPBFed samples [10].

#### 3.6.2. Isothermal magnetisation

The initial M-H curves in Fig. 15a-c and Fig. 15d-f show the magnetization dynamics near the martensite transition temperature (T$_M$) and $T_C^A$, respectively for the three samples, where, the isothermal magnetisation process was taken at two steps every 5 K (from 0 to 1 T, then back to 0 T.) Around T$_M$, a small magnetic hysteresis is observed within the temperature range 135–195 K for the No.1 sample, 115–160 K for the No.2 sample, and 125–195 K for the No.3 sample, which is a nature of the FOPT as a result of the structural transformation that occurs within these temperature ranges, in agreement with Raji [42]. The M-H curves in Fig. 15d-f exhibit FM-paramagnetic (PM) transition of austenite around $T_C^A$, where below $T_C^A$, the magnetisation increases linearly with the applied magnetic field and then saturates at ~ 0.1 T, which is a characteristic of ferromagnetism. Meanwhile above $T_C^A$, the magnetisation increases linearly with the applied magnetic field in correspondence with the paramagnetism [42]. To determine the nature of each magnetic transition, the induced Arrott plots were employed as in Fig. 16. Where the positive and negative slope of Arrott plots around the transition temperature indicates SOPT and FOPT, respectively [43]. Accordingly, this reveals the SOPT nature around $T_C^A$ (Fig. 16d-f), meanwhile, it is not the case around T$_M$ that shows also positive Arrott plots but with FOPT. The FOPT around T$_M$ is probably weak but can be confirmed by the existing magnetic hysteresis in M-H and Arrott plots, which is a character of the FOPT (Fig. 16a-c), in agreement with [34]. The suppression/weakness of the FOPT arises from the existing inhomogeneity MnO segregation, see Fig. 11 and the presence of the orthorhombic 4 O-type martensite phase (See Fig. 13). It can be seen in Fig. 14 and Fig. 16, the $T_C^A$ of the No.1 sample and No.3 sample was approximately 320 K, while the $T_C^A$ of the No.2 sample increased marginally to 323 K. Because the No.1 and No.3 samples saw higher Ni content (see Table 5). The $T_C^A$ decreased with increasing Ni atoms because Ni has a lower magnetic moment than Mn the substitution of Ni atoms for Mn resulted in the dilution of the magnetic
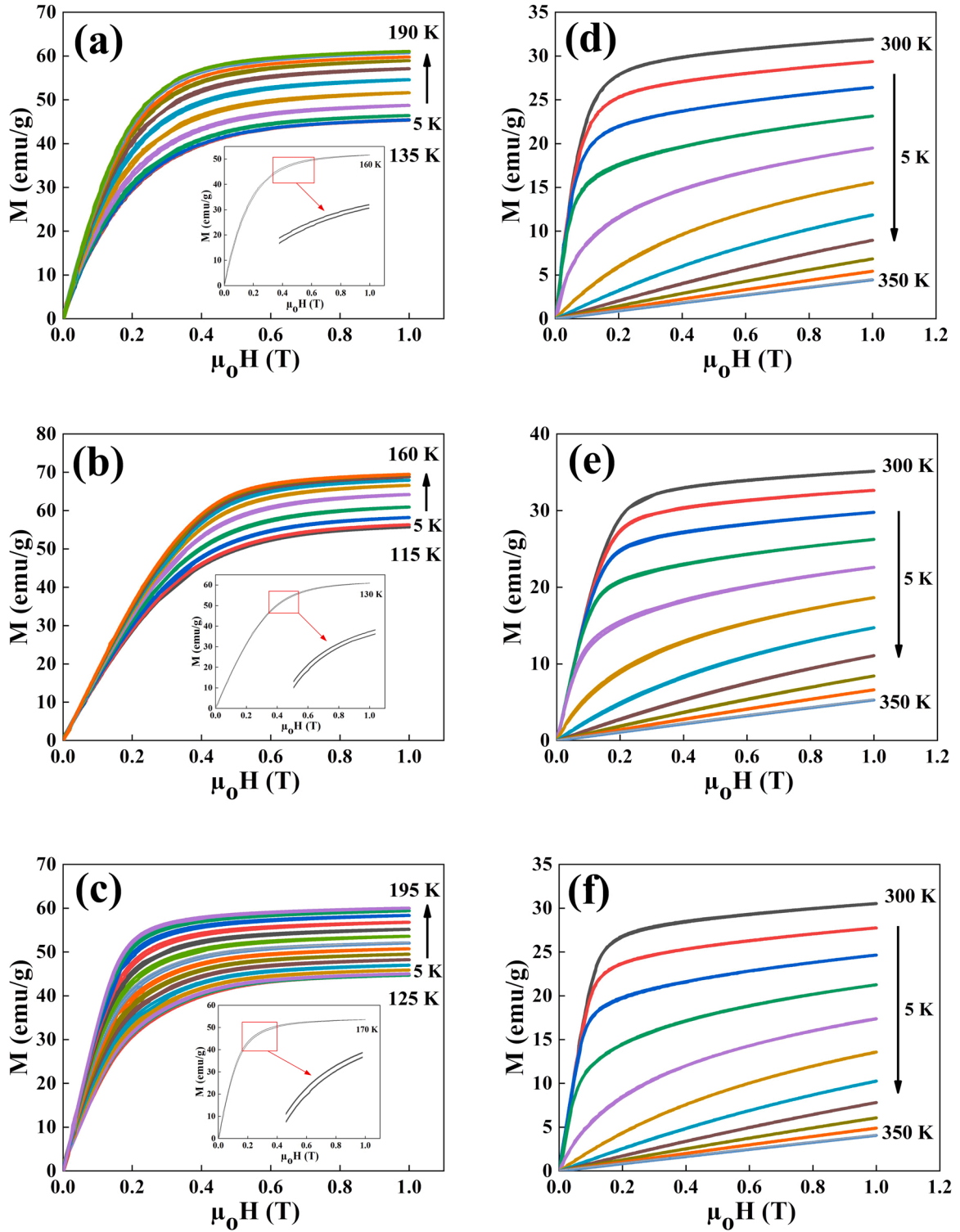
**Fig. 15.** (a, b, c) Isothermal magnetisation curves of HT LPBFed block samples with E = 18.52 J/mm³, 53.33 J/mm³ and 88.89 J/mm³ near the martensitic transition temperature, (d,e,f) Isothermal magnetization curves of HT LPBFed block samples with E = 18.52 J/mm³, 53.33 J/mm³, and E = 88.89 J/mm³ near the $T_C^A$.

subsystem in the austenite phase [30]. The nature of magnetic transition can also be confirmed by the $\Delta S$ dependence on the magnetic field in Eq. 5 [44], where Fig. 17 shows that the value of **n** constant is below 2, which is the case of SOPT around both $T_C^A$ and $T_M$ [45,46].

$$\Delta S \alpha H^n \tag{5}$$

### 3.6.3. Magnetocaloric effect (MCE)

The experimental results show that the start temperature of martensite (Ms) is very sensitive to chemical composition [47]. The three samples showed different Ms, due to the different valence electron concentrations per atom (e/a; determined as the concentration-weighted sum of s, d, and p valence electrons [24,48]), caused by different chemical compositions, as presented in Table 5. The No.2 sample had the lowest Ms because of the lower density of the
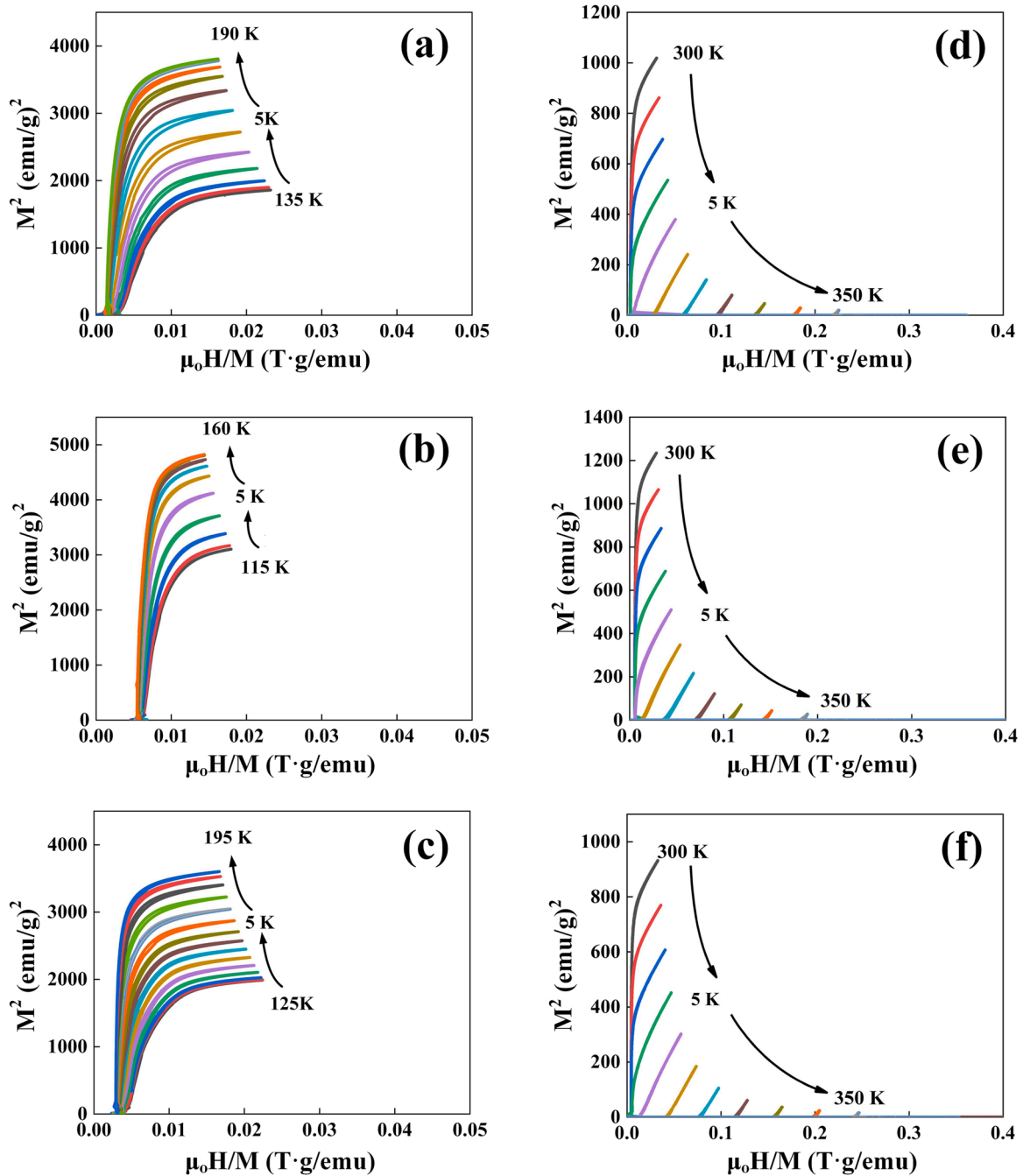
**Fig. 16.** Arrott plots of HT LPBFed block samples with E = 18.52 J/mm$^3$, 53.33 J/mm$^3$, and E = 88.89 J/mm$^3$ near (a,b,c) the martensitic transition temperature and (d, e, f) near the $T_C^A$.

valance electron number [24]. When the valance electron number increase, the energy of the system increase because the energy conduction electrons exceed the Fermi level and move to the corners of the Brillouin zone [49,50]. The system tends to minimize the free energy by creating distortions and generating the new crystal structure, which is the martensite transition [49,50]. In addition, Ms also decreased as the lattice parameter increased [24,51,52]. When the Sn content of the No.2 sample was increased to 17.29% the lattice parameter increased leading to a decrease in Ms [24].

The MCE is an intrinsic property of Ni-Mn-based HAs [53]. To evaluate this characteristic in the vicinity of FOPT and SOPT, the reversible change of magnetic entropy ($\Delta S$) can be quantified from the magnetisation versus magnetic field (M–H) curves at various temperatures using Maxwell's relation (Eq.3). Fig. 18 shows $\Delta S$ as a function of

temperature when applied 1 Tesla (T) fields around the martensitic transition region and the $T_C^A$ range for the three samples with different parameters. The maximum magnetic entropy change ($\Delta S_{max}$) values of FOPT are 0.53 Jkg$^{-1}$ K$^{-1}$ at 160 K, 0.5 Jkg$^{-1}$ K$^{-1}$ at 130 K, and 0.3 Jkg$^{-1}$ K$^{-1}$ at 170 K for the No.1, No.2, and No.3 samples, respectively. And $\Delta S_{max}$ of almost 1.0 Jkg$^{-1}$ K$^{-1}$ at $T_C^A$ (~320 K) for the three HT LPBFed samples (see Fig. 18b).

It is worth mentioning that the obtained results are lower than the recently published results of LPBF Ni$_{45}$Mn$_{44}$Sn$_{11}$ [10]. This is due to the use of pre-alloyed powder that results in more homogeneity and strong FOPT. The study reported that the homogenised LPBFed Ni$_{45}$Mn$_{44}$Sn$_{11}$ alloys exhibited a FOPT, and the maximal value of $\Delta S$ is ≈ 1.3 Jkg$^{-1}$ K$^{-1}$ at 1 T magnetic field [10]. Table 7 shows a comparison between the
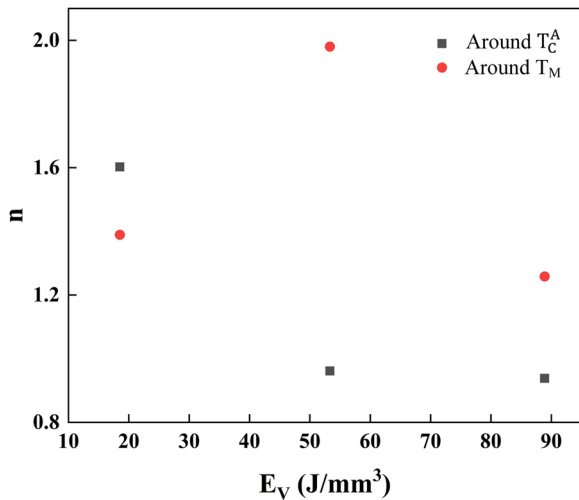
**Fig. 17.** The value of n around the $T_C^A$ and $T_M$.

results of this work and previous works of Ni-Mn-Sn HAs. It is obvious that the $\Delta S_{max}$ in this work is lower than other reports. The difference in the $\Delta S_{max}$ was caused by the large amount of segregation within the HT LPBF samples. The LPBF process of in situ powder inevitably results in elemental segregations, as shown in Figs. 5–7 and Fig. 11. The segregations (Ni and Mn) cannot be reversed with future HT procedures, and has a detrimental effect on the magnetic properties of the alloy. In addition, the different chemical compositions in the annealed LPBF samples can affect structural transition. In Fig. 13, the XRD result of the No.2 sample at low temperatures showed a little Martensite phase. It is obvious that the $\Delta S_{max}$ of SOPT in this work is better than some reports, as shown in Table 7. The $T_C^A$ of the samples only changed marginally. The above results conclude that the different LPBF process parameters didn't significantly affect the $\Delta S$ value around $T_C^A$. Because the $T_C^A$ is insensitive to the changes in the Mn/Z ratio and remains close to RT in Ni$_2$Mn$_{1+x}$Z$_{1-x}$ (Z = In, Sn, Sb) series [54]. The FM order is almost fully defined by the positive exchange interactions between the Mn and Ni atoms, which always constitute the same number of nearest neighbours [54]. Another factor in measuring the MCE efficiency is the RCP as calculated and shown in Table 7. The RCP at $T_C^A$ of the three samples is similar (about 27.5 J kg$^{-1}$). However, the RCP at $T_M$ of the three samples saw a difference. Although $\Delta S_{max}$ of No.3 is the lowest, the RCP of No.3 shows higher value (17.86 J kg$^{-1}$) because of the broad working temperature. The high RCP implies great cooling efficiency.

## 4. Conclusion
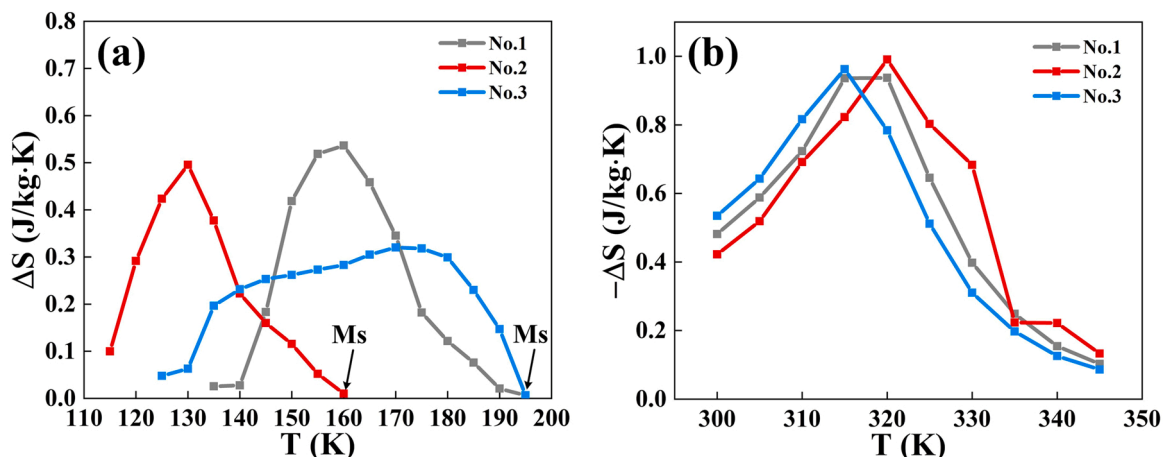
This study investigated the LPBF of Ni-Mn-Sn-based Heusler alloys with different shapes, blocks, MC cylinders and lattices. The density increases with increasing E$_V$ reaching an average value of ~8.3 g/cm$^3$. The LPBF processing parameters were optimised where the optimuim condition for the blocks was defined as EV = 53.33 J/mm$^3$ (P = 80 W, v=1000 m/s and h=0.05 mm). The low laser powers (60, 70 and 80 W) with low energy density are more suitable for manufacturing MC cylinders and lattices when using the 90° raster scan strategy. The AF parts were homogenised by heat treatment for 504 h and then quenched in water. The XRD has shown the L2$_1$ phase for all samples with a minor 4 O orthorhombic phase. The samples showed also double magnetic transitions, martensitie-austenite transition, and curie temperature. The maximum magnetic entropy change ($\Delta S_{max}$) values of the three samples around T$_M$ are 0.53 Jkg$^{-1}$ K$^{-1}$ at 160 K, 0.5 Jkg$^{-1}$ K$^{-1}$ at 130 K, and 0.3 Jkg$^{-1}$ K$^{-1}$ at 170 K, respectively. The different LPBF process parameters didn't significantly affect the $\Delta S$ value around $T_C^A$ because it was insensitive to changes in the Mn/Sn ratio. The $\Delta Smax$ for the three LPBF samples around $T_C^A$ (~320 K) is approximately 1.0 Jkg$^{-1}$ K$^{-1}$ when applied to the 1 T field. The results demonstrated that it is possible to successfully produce 3D printed Ni-Mn-Sn Heusler alloy magnetic refrigerant with acceptable MCE efficiency. Although the MCE efficiency of the LPBF block samples was lower than the alloy manufactured using arc melting, it is predicted that the MCE of LPBF samples can be increased by using the pre-alloy powder. Furthermore, The cracking problem of LPBFed Ni-Mn-Sn HAs needs to be solved. Heat exchangers with the more large surface area should be manufactured to increase the efficiency of heat exchange. The structures in this work will also be used in a mini heat exchanger prototype to improve the cooling performance. The heat treatment processes will be studied to improve the magnetic refrigeration of LPBFed Ni-Mn-Sn alloys.

## CRediT authorship contribution statement

**Kun Sun:** Writing – original draft, Visualization, Validation, Software, Methodology, Investigation, Formal analysis, Data curation, Conceptualization. **Abd El-Moez A. Mohamed:** Writing – review & editing, Supervision, Methodology, Investigation, Formal analysis. **Sheng Li:** Writing – review & editing, Methodology. **Minki Jeong:** Investigation. **Jake Head:** Investigation. **Moataz M. Attallah:** Supervision, Project administration, Funding acquisition, Conceptualization, Writing - review & editing.



**Fig. 18.** (a) Thermal variation of ΔS around FOPT of HT block samples at 1 T, and (b) Thermal variation of ΔS around SOPT of HT block samples at 1 T.

**Table 7**

Comparison of the magnetic entropy of the Ni-Mn-Sn Heusler alloys with those reported in the literature.

| Alloy | Applied Field (T) | $-\Delta S_{max}$ of SOPT (J kg$^{-1}$ K$^{-1}$) | $\Delta S_{max}$ of FOPT ( J kg$^{-1}$ K$^{-1}$) | RCP at $T_C^A$ (J/kg) | RCP at $T_M$ (J/kg) | Manufactured method | Reference |
|---|---|---|---|---|---|---|---|
| Ni$_{49.14}$Mn$_{34.7}$Sn$_{16.16}$ | 1 | 0.94 | 0.5 | 27.27 | 13.73 | Additive manufacturing in-suit powder & | This work |
| Ni$_{48.8}$Mn$_{33.91}$Sn$_{17.29}$ | 1 | 0.99 | 0.53 | 27.94 | 9.74 | 950 ℃ for 504 h & Quench | This work |
| Ni$_{49.25}$Mn$_{34.22}$Sn$_{16.53}$ | 1 | 0.96 | 0.3 | 27.56 | 17.86 | | This work |
| Ni$_{45}$Mn$_{44}$Sn$_{11}$ | 1.5 | / | 2.1 | / | / | Additive manufacturing pre-alloy powder & 1173 K for 24 h & Quench | [10] |
| Ni$_{45}$Mn$_{44}$Sn$_{11}$ | 5 | 4 | 15 | 34 | 71 | Arc melting & 1273 K for 24 h & quenched in ice water | [55] |
| Ni$_{50}$Mn$_{35}$Sn$_{15}$ | 5 | 2.105 | / | 132.5 | / | Arc melting & Melt-spun ribbons 40 m/s | [56] |
| Ni$_{2.12}$Mn$_{1.28}$Sn$_{0.6}$ | 5 | ~2 | 10.2 | / | 80 | Arc melting & 1173 K for 24 h & slowly cooled down | [30] |
| Ni$_{2.18}$Mn$_{1.22}$Sn$_{0.6}$ | 5 | 5.9 | 2.16 | / | 89 | Arc melting & 1173 K for 24 h & slowly cooled down | [30] |
| Ni$_{47}$Mn$_{40}$Sn$_{13}$ | 5 | / | 7.5 | 207 | 62 | Mechanical alloying & 1223 K for 16 h & quenched in ice-water | [57] |
| Ni$_{48}$Mn$_{39.5}$Sn$_{12.5}$ | 2 | 1.8 | 7.8 | 92.1 | 55.5 | Melt-spun ribbons (25 m/s) | [58] |
| Ni$_{50}$Mn$_{37}$Sn$_{13}$ | 1.2 | 1.1 | 1.9 | / | / | As melted & 1123 K for 4 h & quenched by Ar-flow | [33] |
| Ni$_{50}$Mn$_{36}$Sn$_{14}$ | 1.2 | ~1.4 | / | / | / | As melted & 1123 K for 4 h & quenched by Ar-flow | [33] |
| Ni$_{50}$Mn$_{35}$Sn$_{15}$ | 1.2 | ~1.2 | / | / | / | As melted & 1123 K for 4 h & quenched by Ar-flow | [33] |
| Ni$_{50}$Mn$_{30}$Sn$_{20}$ | 1.2 | ~1.3 | / | / | / | As melted & 1123 K for 4 h & quenched by Ar-flow | [33] |
| Ni$_{50}$Mn$_{20}$Sn$_{30}$ | 1.2 | ~1.12 | / | / | / | As melted & 1123 K for 4 h & quenched by Ar-flow | [33] |
| Ni$_{50}$Mn$_{35}$Sn$_{15}$ | 5 | / | 15 | / | / | Arc melting & 1273 K for 2 h & quenched in ice water | [32] |
| Ni$_{50}$Mn$_{37}$Sn$_{13}$ | 5 | ~1.8 | 18 | / | / | Arc melting & 1273 K for 2 h & quenched in ice water | [32] |
| Ni$_{50}$Mn$_{25}$Sn$_{25}$ | 2 | 1.4 | / | / | / | Hybrid microwave heating method | [59] |
| Ni$_{43}$Mn$_{46}$Sn$_{11}$ | 5 | / | 43.2 | / | / | Arc melting & melt spun ribbons & 1173 K for 10 min | [60] |

## Declaration of Competing Interest

## Data Availability

Data will be made available on request.

## Acknowledgments

## References

[1] V. Franco, J.S. Blazquez, B. Ingale, A. Conde, The magnetocaloric effect and magnetic refrigeration near room temperature: materials and models, Annu. Rev. Mater. Res. 42 (2012) 305–342.

[2] V. Chaudhary, X. Chen, R.V. Ramanujan, Iron and manganese based magnetocaloric materials for near room temperature thermal management, Prog. Mater. Sci. 100 (2019) 64–98.

[3] V. Franco, J.S. Blazquez, J.J. Ipus, J.Y. Law, L.M. Moreno-Ramirez, A. Conde, Magnetocaloric effect: from materials research to refrigeration devices, Prog. Mater. Sci. 93 (2018) 112–232.

[4] S.Y. Dan`kov, A.M. Tishin, V.K. Pecharsky, K.A. Gschneidner, Magnetic phase transitions and the magnetothermal properties of gadolinium, Phys. Rev. B 57 (6) (1998) 3478–3490.

[5] P. Shamba, N.A. Morley, O. Cespedes, I.M. Reaney, W.M. Rainforth, Optimization of magnetocaloric properties of arc-melted and spark plasma-sintered LaFe11.6Si1.4, Appl. Phys. A 122 (8) (2016) 732.

[6] Z. Zhong, S. Ma, D. Wang, Y. Du, A review on the regulation of magnetic transitions and the related magnetocaloric properties in Ni-Mn-Co-Sn alloys, J. Mater. Sci. Technol. 28 (3) (2012) 193–199.

[7] A.E.-M.A. Mohamed, B. Hernando, Self-assembled impurity and its effect on magnetic and magnetocaloric properties of manganites, Ceram. Int 44 (14) (2018) 17044–17049.

[8] J.D. Moore, D. Klemm, D. Lindackers, S. Grasemann, R. Träger, J. Eckert, L. Löber, S. Scudino, M. Katter, A. Barcza, K.P. Skokov, O. Gutfleisch, Selective laser melting of La(Fe,Co,Si)13 geometries for magnetic refrigeration, J. Appl. Phys. 114 (4) (2013), 043907.

[9] T. DebRoy, H.L. Wei, J.S. Zuback, T. Mukherjee, J.W. Elmer, J.O. Milewski, A. M. Beese, A. Wilson-Heid, A. De, W. Zhang, Additive manufacturing of metallic components – Process, structure and properties, Prog. Mater. Sci. 92 (2018) 112–224.

[10] W. Sun, X. Lu, Z. Wei, Q. Li, Z. Li, Y. Zhang, J. Liu, Multicaloric effect in Ni–Mn–Sn metamagnetic shape memory alloys by laser powder bed fusion, Addit. Manuf. 59 (2022), 103125.

[11] A.E.-M.A. Mohamed, M. Jeong, R.S. Sheridan, M.M. Attallah, Enabling high efficiency magnetic refrigeration using laser powder bed fusion of porous LaCe(Fe, Mn,Si)13 structures, Addit. Manuf. 51 (2022), 102620.

[12] V. Chaudhary, S.A. Mantri, R.V. Ramanujan, R. Banerjee, Additive manufacturing of magnetic materials, Prog. Mater. Sci. 114 (2020), 100688.

[13] B.T. Lejeune, R. Barua, E. Simsek, R.W. McCallum, R.T. Ott, M.J. Kramer, L. H. Lewis, Towards additive manufacturing of magnetocaloric working materials, Materialia 16 (2021), 101071.

[14] M.S.K.K.Y. Nartu, A. Jagetia, V. Chaudhary, S.A. Mantri, E. Ivanov, N.B. Dahotre, R.V. Ramanujan, R. Banerjee, Magnetic and mechanical properties of an additively manufactured equiatomic CoFeNi complex concentrated alloy, Scr. Mater. 187 (2020) 30–36.

[15] V. Chaudhary, M.S.K.K.Y. Nartu, S. Dasari, S.M. Varahabhatla, A. Sharma, M. Radhakrishnan, S.A. Mantri, S. Gorsse, N.B. Dahotre, R.V. Ramanujan, R. Banerjee, Magnetic and mechanical properties of additively manufactured Alx (CoFeNi) complex concentrated alloys, Scr. Mater. 224 (2023), 115149.

[16] W.H. Teh, V. Chaudhary, S. Chen, S.H. Lim, F. Wei, J.Y. Lee, P. Wang, S.P. Padhy, C.C. Tan, R.V. Ramanujan, High throughput multi-property evaluation of additively manufactured Co-Fe-Ni materials libraries, Addit. Manuf. 58 (2022), 102983.

[17] C. Shen, K.-D. Liss, M. Reid, Z. Pan, X. Hua, F. Li, G. Mou, Y. Huang, Y. Zhu, H. Li, Fabrication of FeNi intermetallic using the wire-arc additive manufacturing process: a feasibility and neutron diffraction phase characterization study, J. Manuf. Process. 57 (2020) 691–699.

[18] X. Miao, W. Wang, H. Liang, F. Qian, M. Cong, Y. Zhang, A. Muhammad, Z. Tian, F. Xu, Printing (Mn,Fe)2(P,Si) magnetocaloric alloys for magnetic refrigeration applications, J. Mater. Sci. 55 (15) (2020) 6660–6668.

[19] Z. Li, N. Zou, C.F. Sánchez-Valdés, J.L. Sánchez Llamazares, B. Yang, Y. Hu, Y. Zhang, C. Esling, X. Zhao, L. Zuo, Thermal and magnetic field-induced

martensitic transformation in Ni50Mn25−xGa25Cux(0 ≤ x ≤ 7) melt-spun ribbons, J. Phys. D: Appl. Phys. 49 (2) (2015), 025002.

[20] K. Navickaitė, J. Liang, C. Bahl, S. Wieland, T. Buchenau, K. Engelbrecht, Experimental characterization of active magnetic regenerators constructed using laser beam melting technique, Appl. Therm. Eng. 174 (2020), 115297.

[21] J. Kagathara, S. Wieland, E. Gärtner, V. Uhlenwinkel, M. Steinbacher, Heat treatment and formation of magnetocaloric 1:13 phase in LaFe11.4Si1.2Co0.4 processed by laser beam melting, Materials 13 (3) (2020) 773.

[22] A. Deltell, A.E.-M.A. Mohamed, P. Álvarez-Alonso, M. Ipatov, J.P. Andrés, J. A. González, T. Sánchez, A. Zhukov, M.L. Escoda, J.J. Suñol, R. López, Martensitic transformation, magnetic and magnetocaloric properties of Ni–Mn–Fe–Sn Heusler ribbons, J. Mater. Res. Technol. 12 (2021) 1091–1103.

[23] I. Titov, M. Acet, M. Farle, D. González-Alonso, L. Mañosa, A. Planes, T. Krenke, Hysteresis effects in the inverse magnetocaloric effect in martensitic Ni-Mn-In and Ni-Mn-Sn, J. Appl. Phys. 112 (7) (2012), 073914.

[24] A. Cakir, L. Righi, F. Albertini, M. Acet, M. Farle, Intermartensitic transitions and phase stability in Ni50Mn50-xSnx Heusler alloys, Acta Mater. 99 (2015) 140–149.

[25] F. Nilsén, I.F. Ituarte, M. Salmi, J. Partanen, S.-P. Hannula, Effect of process parameters on non-modulated Ni-Mn-Ga alloy manufactured using powder bed fusion, Addit. Manuf. 28 (2019) 464–474.

[26] K.G. Prashanth, S. Scudino, T. Maity, J. Das, J. Eckert, Is the energy density a reliable parameter for materials synthesis by selective laser melting? Mater. Res. Lett. 5 (6) (2017) 386–390.

[27] Standard Test Methods for Density of Compacted or Sintered Powder Metallurgy (PM) Products Using Archimedes, Principle, ASTM B962 e 17.

[28] C.A. Schneider, W.S. Rasband, K.W. Eliceiri, NIH Image to ImageJ: 25 years of image analysis, Nat. Methods 9 (7) (2012) 671–675.

[29] C. Tan, S. Li, K. Essa, P. Jamshidi, K. Zhou, W. Ma, M.M. Attallah, Laser powder bed fusion of Ti-rich TiNi lattice structures: process optimisation, geometrical integrity, and phase transformations, Int. J. Mach. Tools Manuf. 141 (2019) 19–29.

[30] M.K. Ray, K. Bagani, S. Banerjee, Effect of excess Ni on martensitic transition, exchange bias and inverse magnetocaloric effect in Ni2+xMn1.4-xSn0.6 alloy, J. Alloy Compd. 600 (2014) 55–59.

[31] K. Fukushima, K. Sano, T. Kanomata, H. Nishihara, Y. Furutani, T. Shishido, W. Ito, R.Y. Umetsu, R. Kainuma, K. Oikawa, K. Ishida, Phase diagram of Fe-substituted Ni–Mn–Sn shape memory alloys, Scr. Mater. 61 (8) (2009) 813–816.

[32] T. Krenke, E. Duman, M. Acet, E.F. Wassermann, X. Moya, L. Mañosa, A. Planes, Inverse magnetocaloric effect in ferromagnetic Ni–Mn–Sn alloys, Nat. Mater. 4 (6) (2005) 450–454.

[33] N.H. Dan, N.H. Duc, N.H. Yen, P.T. Thanh, L.V. Bau, N.M. An, D.T.K. Anh, N. A. Bang, N.T. Mai, P.K. Anh, T.D. Thanh, T.L. Phan, S.C. Yu, Magnetic properties and magnetocaloric effect in Ni-Mn-Sn alloys, J. Magn. Magn. Mater. 374 (2015) 372–375.

[34] H.C. Xuan, Q.Q. Cao, C.L. Zhang, S.C. Ma, S.Y. Chen, D.H. Wang, Y.W. Du, Large exchange bias field in the Ni–Mn–Sn Heusler alloys with high content of Mn, Appl. Phys. Lett. 96 (20) (2010), 202502.

[35] T. Krenke, M. Acet, E.F. Wassermann, X. Moya, L. Mañosa, A. Planes, Martensitic transitions and the nature of ferromagnetism in the austenitic and martensitic states of Ni-Mn-Sn alloys, Phys. Rev. B 72 (1) (2005), 014412.

[36] G. Kirat, O. Kizalaslan, M.A. Aksan, Magnetocaloric properties of Ni-Rich Ni50-xCoxMn38Sn12B3 shape memory ribbons, J. Supercond. Nov. Magn. 34 (2) (2021) 581–588.

[37] C. Garcia, V. Zhukova, S. Shevyrtalov, M. Ipatov, P. Corte-Leon, A. Zhukov, Tuning of magnetic properties in Ni-Mn-Ga Heusler-type glass-coated microwires by annealing, J. Alloy Compd. 838 (2020), 155481.

[38] J.D. Santos, T. Sanchez, P. Alvarez, M.L. Sanchez, J.L. Sánchez Llamazares, B. Hernando, L. Escoda, J.J. Suñol, R. Varga, Microstructure and magnetic properties of Ni50Mn37Sn13 Heusler alloy ribbons, J. Appl. Phys. 103 (7) (2008) 07B326.

[39] J. Mohanty, A. Persson, D. Arvanitis, K. Temst, C. Van Haesendonck, Direct observation of frozen moments in the NiFe/FeMn exchange bias system, N. J. Phys. 15 (3) (2013), 033016.

[40] P.J. Brown, A.P. Gandy, K. Ishida, R. Kainuma, T. Kanomata, K.U. Neumann, K. Oikawa, B. Ouladdiaf, K.R.A. Ziebeck, The magnetic and structural properties of the magnetic shape memory compound Ni2Mn1.44Sn0.56, J. Phys.: Condens. Matter 18 (7) (2006) 2249–2259.

[41] X. Zhang, H. Zhang, M. Qian, L. Geng, Enhanced magnetocaloric effect in Ni-Mn-Sn-Co alloys with two successive magnetostructural transformations, Sci. Rep. -Uk 8 (1) (2018) 8235.

[42] G.R. Raji, A.P. Paulose, R.B. Job, S. Thomas, K.G. Suresh, M.R. Varma, Phase transformations, inverse magnetocaloric effect and critical behavior of Ni50Mn36Sn14-xSix Heusler alloys, Intermetallics 82 (2017) 59–67.

[43] B.J.Pl Banerjee, 1964. On a generalised approach to first and second order magnetic transitions, Phys. Lett. 12(1) (1964) 16–17.

[44] T.D. Shen, R.B. Schwarz, J.Y. Coulter, J.D. Thompson, Magnetocaloric effect in bulk amorphous Pd40Ni22.5Fe17.5P20 alloy, J. Appl. Phys. 91 (8) (2002) 5240–5245.

[45] J.Y. Law, V. Franco, L.M. Moreno-Ramírez, A. Conde, D.Y. Karpenkov, I. Radulov, K.P. Skokov, O. Gutfleisch, A quantitative criterion for determining the order of magnetic phase transitions using the magnetocaloric effect, Nat. Commun. 9 (1) (2018) 2680.

[46] F. Chen, J.L. Sánchez Llamazares, C.F. Sánchez-Valdés, F. Chen, Z. Li, Y.X. Tong, L. Li, Large magnetic entropy change and refrigeration capacity around room temperature in quinary Ni41Co9-xFexMn40Sn10 alloys (x= 2.0 and 2.5), J. Alloys and Compd. 825 (2020), 154053.

[47] V. Chernenko, E. Cesari, V. Kokorin, I. Vitenko, The development of new ferromagnetic shape memory alloys in Ni-Mn-Ga system, Scr. Metall. Et. Mater. 33 (8) (1995) 1239–1244.

[48] T. Krenke, Untersuchung der martensitischen Umwandlung und der magnetischen Eigenschaften Mangan-reicher Ni-Mn-In-und Ni-Mn-Sn-Heusler-Legierungen, in: Dissertation, University Duisburg-Essen, 2007.

[49] X.Q. Chen, F.J. Yang, X. Lu, Z.X. Qin, 2007. The way composition affects martensitic transformation temperatures of Ni–Mn–Ga Heusler alloys, physic. stat. solid. B 244(3) (2007) 1047–1053.

[50] V.A. Chernenko, Compositional instability of β-phase in Ni-Mn-Ga alloys, Scr. Mater. 40 (5) (1999) 523–527.

[51] X. Jin, M. Marioni, D. Bono, S.M. Allen, R.C. O'Handley, T.Y. Hsu, Empirical mapping of Ni–Mn–Ga properties with composition and valence electron concentration, J. Appl. Phys. 91 (10) (2002) 8222–8224.

[52] C. Jiang, G. Feng, S. Gong, H. Xu, Effect of Ni excess on phase transformation temperatures of NiMnGa alloys, Mater. Sci. Eng.: A 342 (1) (2003) 231–235.

[53] J.R. Gomez, R.F. Garcia, A.D. Catoira, M.R. Gomez, Magnetocaloric effect: a review of the thermodynamic cycles in magnetic refrigeration, Renew. Sust. Energy Rev. 17 (2013) 74–82.

[54] S. Singh, L. Caron, S.W. D'Souza, T. Fichtner, G. Porcari, S. Fabbrici, C. Shekhar, S. Chadov, M. Solzi, C. Felser, Large magnetization and reversible magnetocaloric effect at the second-order magnetic transition in Heusler materials, Adv. Mater. 28 (17) (2016) 3321–3325.

[55] T. Chabri, A. Venimadhav, T.K. Nath, Interplay of austenite and martensite phase inside martensite transition regime and its role on magnetocaloric effect and magnetoresistance in Ni-Mn-Sn based Heusler alloy, Intermetallics 102 (2018) 65–71.

[56] K. Dadda, S. Alleg, S. Souilah, J.J. Sunol, E. Dhahri, L. Bessais, E.K. Hlil, Critical behavior, magnetic and magnetocaloric properties of melt-spun Ni50Mn35Sn15 ribbons, J. Alloy Compd. 735 (2018) 1662–1672.

[57] A.G. Varzaneh, P. Kameli, T. Amiri, K.K. Ramachandran, A. Mar, I.A. Sarsari, J. L. Luo, T.H. Etsell, H. Salamati, Effect of Cu substitution on magnetocaloric and critical behavior in Ni47Mn40Sn13-xCux alloys, J. Alloy Compd. 708 (2017) 34–42.

[58] P. Czaja, W. Maziarz, J. Przewoznik, C. Kapusta, L. Hawelek, A. Chrobak, P. Drzymala, A. Fitta, A. Kolano-Burian, Magnetocaloric properties and exchange bias effect in Al for Sn substituted Ni48Mn39.5Sn12.5 Heusler alloy ribbons, J. Magn. Magn. Mater. 358 (2014) 142–148.

[59] L. Trombi, F. Cugini, R. Rosa, N.S. Amadè, S. Chicco, M. Solzi, P. Veronesi, Rapid microwave synthesis of magnetocaloric Ni–Mn–Sn Heusler compounds, Scr. Mater. 176 (2020) 63–66.

[60] Y. Zhang, L. Zhang, Q. Zheng, X. Zheng, M. Li, J. Du, A. Yan, Enhanced magnetic refrigeration properties in Mn-rich Ni-Mn-Sn ribbons by optimal annealing, Sci. Rep. -Uk 5 (1) (2015) 11010.